Available online at www.sciencedirect.com
ScienceDirect
Trans. Nonferrous Met. Soc. China 33(2023) 1687−1700
Transactions of Nonferrous Metals Society of China
www.tnmsc.cn

Microstructure evolution and mechanical properties of Al−Mg−Sc−Zr alloy sheet after friction stir welding

Jing-yu JIANG[1], Feng JIANG[2,3,4], Meng-han ZHANG[2]

1. School of Metallurgy and Environment, Central South University, Changsha 410083, China;
2. School of Materials Science and Engineering, Central South University, Changsha 410083, China;
3. Light Alloy Research Institute, Central South University, Changsha 410083, China;
4. National Key Laboratory of Science and Technology for National Defence on High-strength Lightweight Structural Materials, Central South University, Changsha 410083, China

Received 8 February 2022; accepted 12 May 2022

Abstract: An Al−Mg−Sc−Zr alloy rolled sheet was subjected to friction stir welding (FSW) with a tool rotation speed of 500 r/min and a tool travel speed of 100 mm/min. The microstructure of the alloy sheet after FSW was characterized by OM, EBSD and TEM. The microhardness and strength were also tested. The results show that after the FSW, the fiber grains adjacent to the rotating tool are bent. The texture of the rolled sheet is gradually alleviated. In the nugget zone, the size of the tiny equiaxed grains is only 2.31 μm. $Al_3(Sc,Zr)$ particles are also affected by the FSW. The distribution and the size of the particles after the FSW are different from those of the original sheet. Moreover, the shape of the $Al_3(Sc,Zr)$ particles turns from spherical to polygonal and many particles become incoherent with the Al matrix. The tensile strength of the FSW sheet is 367 MPa and the yield strength is 263 MPa, and those of the original sheet are 414 and 311 MPa.

Key words: Al−Mg−Sc−Zr alloy; friction stir welding; dynamic recrystallization; $Al_3(Sc,Zr)$ particles; strength

1 Introduction

Al−Mg alloys are widely used in transportation and aerospace industries due to medium-strength, low density, satisfactory corrosion resistance and especially excellent weld ability [1−3]. By adding a small amount of Sc and Zr to the Al−Mg alloy, the strength can be elevated while the corrosion resistance and the weld ability can still be maintained due to the pinning effect of extremely fine and coherent $Al_3(Sc,Zr)$ particles with $L1_2$ structure, which can effectively refine grains and inhibit recrystallization [4−7]. These advantages make the new type Al−Mg−Sc−Zr alloy gradually become a potential material in aerospace engineering. During the processing and preparation of metal materials, welding is an indispensable process in most cases. For Al alloy, welding methods include tungsten inert gas welding (TIGW), metal inert-gas welding (MIGW), electron beam welding (EBW) and variable polarity plasma arc welding (VPPAW) [8−11]. These welding methods all belong to fusion welding, which uses heat to melt the welding wire and the weld part to fuse the workpieces together. Therefore, the center of weld zone likes a cast structure, leading to its comparably low strength [8]. In addition, these fusion welding methods may introduce defects to the weld center such as pores and hot-crackings [12], which would probably undermine the weld property.

In recent years, friction stir welding (FSW) gradually becomes an important welding method for Al alloys [13]. Different from the fusion welding

Corresponding author: Feng JIANG, Tel: +86-13787009528, E-mail: jfeng2@csu.edu.cn
DOI: 10.1016/S1003-6326(23)66214-4

methods, FSW is a solid-state joining technology, connecting the materials by the thermoplasticity. During FSW process, a rotating probe with a special pin and a shoulder is plunged into the gap of the work-pieces and moved along the weld joint. Through the friction between the rotating tool and the material, heat is generated and the material is softened, thus, the work-pieces are connected by thermoplastic deformation. The lower heat input results in better mechanical properties, and less possibility of distortions in the part and in the welded region [14]. Because of the special mechanism of FSW, the grain size in welding center is very small [15], and it can also be regarded as a kind of severe plastic deformation (SPD). Therefore, friction stir processing (FSP), which is derived from FSW, becomes a new important method of grain refinement, and some researchers have studied the microstructure and properties of FSWed/FSPed Al alloys [16−25]. For example, TAO et al [23] have researched the influence of welding parameter on microstructure of Al–Mg–Sc FSW joints. It has found that with the increase of travel speed and the decrease of the rotation rate, the grain size would decrease. MALOPHEYEV et al [24] found that Al−Mg−Sc FSW joints enjoy high level of welding efficiency, especially in the annealed sample (nearly 100%). Meanwhile, the joint efficiency of TIGW is only 70%. In addition, VYSOTSKIY et al [25] studied the effect of FSP on the properties of the Al−Mg−Sc alloy cast ingot, and found that the strength of the FSPed ingot has been obviously improved. However, the previous researches are mainly concerned on welding parameters, mechanical properties and fractures. Studies on the important precipitation $Al_3(Sc,Zr)$, which is a key factor affecting the Al−Mg−Sc−Zr alloy, are not enough. KALASHNIKOVA et al [26] found that the weld zone of a FSWed Al−Mg−Sc−Zr alloy was fine-grained but had a microhardness less than that of the base material, which may be explained by the over-aging effect of FSW on the $Al_3(Sc,Zr)$ precipitates. In addition, many studies show that SPD may lead to the change of size and morphology of $Al_3(Sc,Zr)$ particles, consequently affecting the property, but the detailed effect on change of $Al_3(Sc,Zr)$ particles by FSW still needs further researches. In order to further study the issues, in this work, the microstructure evolution, the $Al_3(Sc,Zr)$ particles and the tensile strength of a FSWed Al−Mg−Sc−Zr alloy sheet were researched carefully, and the mechanisms were discussed systematically, especially the $Al_3(Sc,Zr)$ particles.

2 Experimental

The material composition is Al−6Mg−0.25Sc−0.1Zr(wt.%). The alloy ingot was first homogenized at 350 °C for 4 h and then treated at 420 °C for 4 h. Then, the ingot was hot rolled by 60% at 350 °C and cold rolled by 80% at room temperature. The rolled sheet was annealed at 280 °C for 1 h to relieve internal stress for the following welding. Subsequently, the sheet was friction stir welded at a tool rotational speed of 500 r/min and a tool travel speed of 100 mm/min. The welding direction (WD) is parallel to the transverse direction (TD). The welding tool was fabricated from a tool steel and consisted of a shoulder of 16 mm in diameter and a threaded probe tapered from 8 mm at the tool shoulder to 4.8 mm at the tip; the probe length was 4 mm. The microstructure and mechanical properties were studied by Vickers hardness (HV), tensile test, optical microscope (OM), electron back-scatter diffraction (EBSD) and transmission electron microscope (TEM). The Vickers hardness was characterized by HVS−100. The hardness test position was along the 1/2 centerline in the thickness direction of the welded joint of the sheet. Before the hardness test, the sample was mechanically ground and polished until the test surface was flat and bright, and a load of 0.1 kg holding for 10 s was loaded for each test. The strength was tested by MTS−810 electronic mechanical testing machine and the rate of tensile testing was 2 mm/min. The sampling location and the dimension of FSW sample are shown in Fig. 1. The metallograph was obtained by Leica DM4000M optical microscope. Specimens for the OM were mechanically polished and then corroded by Keller's reagent (95% H_2O + 2.5% HNO_3 + 1.5% HCl + 1% HF) for 30 s. SEM was carried out on JSM−7900F. Specimens for the EBSD were mechanically polished, followed by an electro-polishing in the solution of HNO_3+CH_3OH with a volume ratio of 1:3 at 253 K, examined by JSM−7900F equipped with an EBSD detector (Oxford, C-Nano) operating at 20 kV. The TEM samples were mechanically polished down to the

thickness of about 90 μm. The final thinning was done by chemical electro-polishing (same as the EBSD), and then characterized by Tecnai G^2 F20 TEM operating at 200 kV.

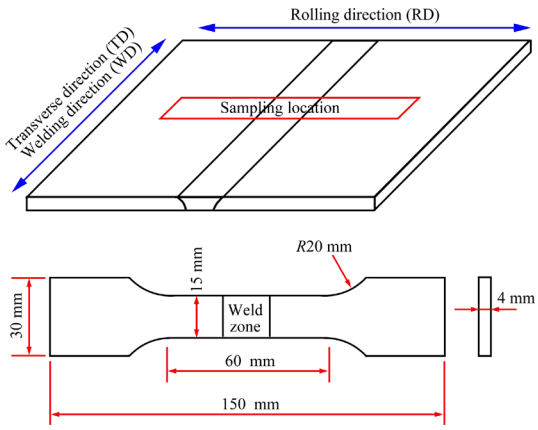

Fig. 1 Dimension of tensile test sample

3 Results

3.1 OM result

Figure 2 shows the overall metallograph of the alloy weld zone. As can be seen from the figure, the welding area is clearly divided into several parts. The center of the weld zone is the nugget zone (NZ). Adjacent to the NZ is the thermomechanically affected zone (TMAZ) where bent fibers can be observed. The outer area is the heat affected zone (HAZ) and base material (BM). To further investigate the detailed microstructure, five points were selected based on the overall OM image for more studies.

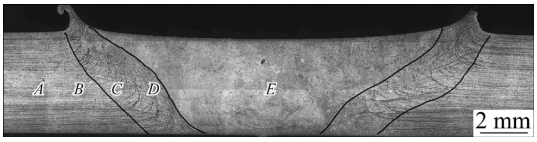

Fig. 2 Overall metallograph of welding area of FSW sample

Figure 3 shows the high magnification images of the three areas *B*, *C* and *D* in Fig. 2. As shown in Fig. 3(a), the left side is the HAZ and the right side is the TMAZ. From the HAZ to the TMAZ, the fiber grains of the sheet are gradually distorted and bent like waves. As the area gets closer to NZ, the fiber structure becomes increasingly convoluted, with a twist angle of about 60° (Fig. 3(b) for region *C*). In the TMAZ near NZ (Fig. 3(c)), the twist angle of the fiber structure exceeds 90°. Moreover, many fine equiaxed grains are mixed in the curved fiber structure.

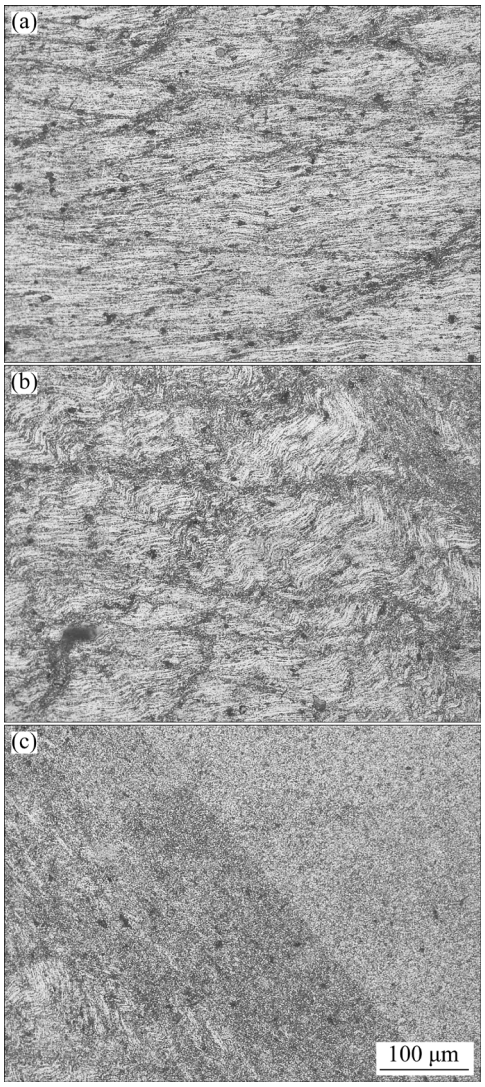

Fig. 3 High magnification images of different areas in Fig. 2 of FSW sample: (a) Area *B*; (b) Area *C*; (c) Area *D*

3.2 EBSD result

Further EBSD analysis has been performed on the five areas *A*, *B*, *C*, *D* and *E* in Fig. 2, and the results are shown in Fig. 4 and Fig. 5. Figure 4(a) shows the BM (Area *A*) of the sample. The microstructure in the figure is mainly fiber grains, and the width of the fiber grains is 3−5 μm. Several little recrystallized grains are found between the fiber grains. There are many low angle GBs (LAGB) in this area and the average grain boundary (GB) angle is 25.62°. In the Area *B*, affected by FSW heat, more tiny recrystallized grains appear at the GBs of fiber grains, but the overall recrystallization

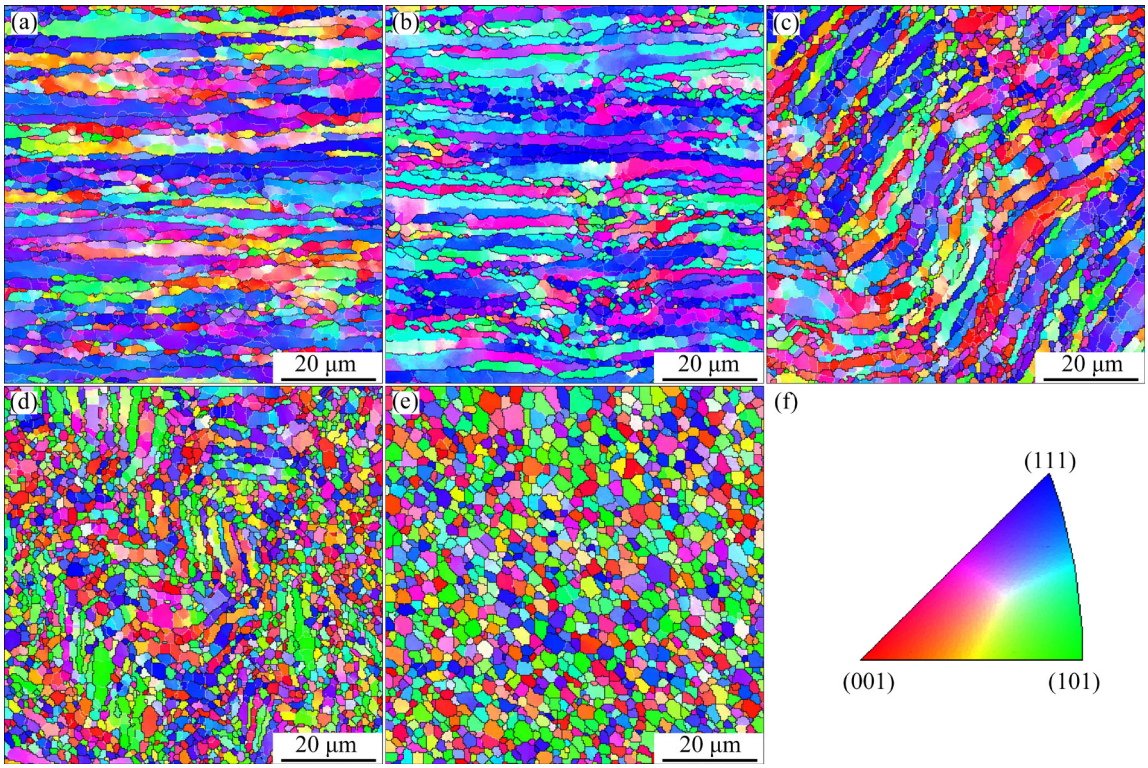

Fig. 4 EBSD results of different areas in Fig. 2: (a) Area *A*; (b) Area *B*; (c) Area *C*; (d) Area *D*; (e) Area *E*; (f) EBSD data

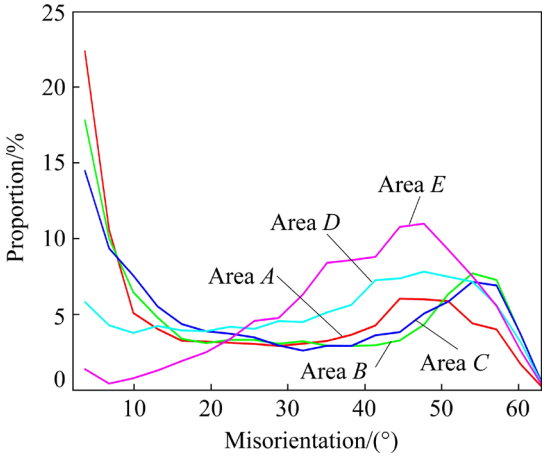

Fig. 5 EBSD grain misorientation of different areas in Fig. 2

degree is still low and the width of the fiber grain does not increase. The average GB angle is 27.41°. Figure 4(c) shows the result of Area *C* in Fig. 2. The fiber grains have been bent by 60°, and more recrystallized grains appear between the fiber grains, and the size of the recrystallized grains is larger than that in the HAZ. The average GB angle rises to 30.32°. However, most of the fiber structure remains continuous even the grains are bent. As the location gets closer to the NZ, the microstructure of the TMAZ changes significantly. As shown in Fig. 4(d), in the TMAZ near NZ (Area *D* in Fig. 2), the bending angle of the fiber grains is greater than 90°, and the bending phenomenon is intenser. The fiber grains are crushed and the continuity has been broken. A large number of equiaxed grains are intercalated between the fractured fiber grains, and the size of these equiaxed grains is larger than that of the Areas *A* and *B*, which indicates that the recrystallization is stronger. In the area adjacent to the NZ (the right side of the Fig. 4(d)), the structure becomes equiaxed grains. The average GB angle rises to 34.27°. Finally, in the NZ (Fig. 4(e)), the structures are all equiaxed grains. The average GB angle rises to 39.05°, and the average grain size is 2.31 μm. Most GBs belong to high angle GBs (HAGB).

As for the orientation evolution, Fig. 6 shows the {111} pole figure from the five EBSD results. In the BM (Fig. 6(a)), brass texture is very obvious, which is consistent with the typical features of rolled sheets. Affected by welding heat, the orientation is slightly changed from the previous area, but its rolling texture is still clear (Fig. 6(b)). However, in the TMAZ, the grain orientations are

different. As shown in Fig. 6(c), although the orientation distribution is still uneven, the orientation of the grains no longer has certain texture characteristics. In the area adjacent to the NZ (Fig. 6(d)), because of the strong thermo-mechanical effect, the original orientation of the rolled sheet totally disappears. The orientation is uniform. The situation is similar in the NZ, and all the grains distribute uniformly in every orientation (Fig. 6(e)).

Furthermore, the recrystallization of each area is also different. The recrystallization results according to the EBSD are shown in Fig. 7 and Fig. 8. For the BM (Fig. 7(a)), the substructure

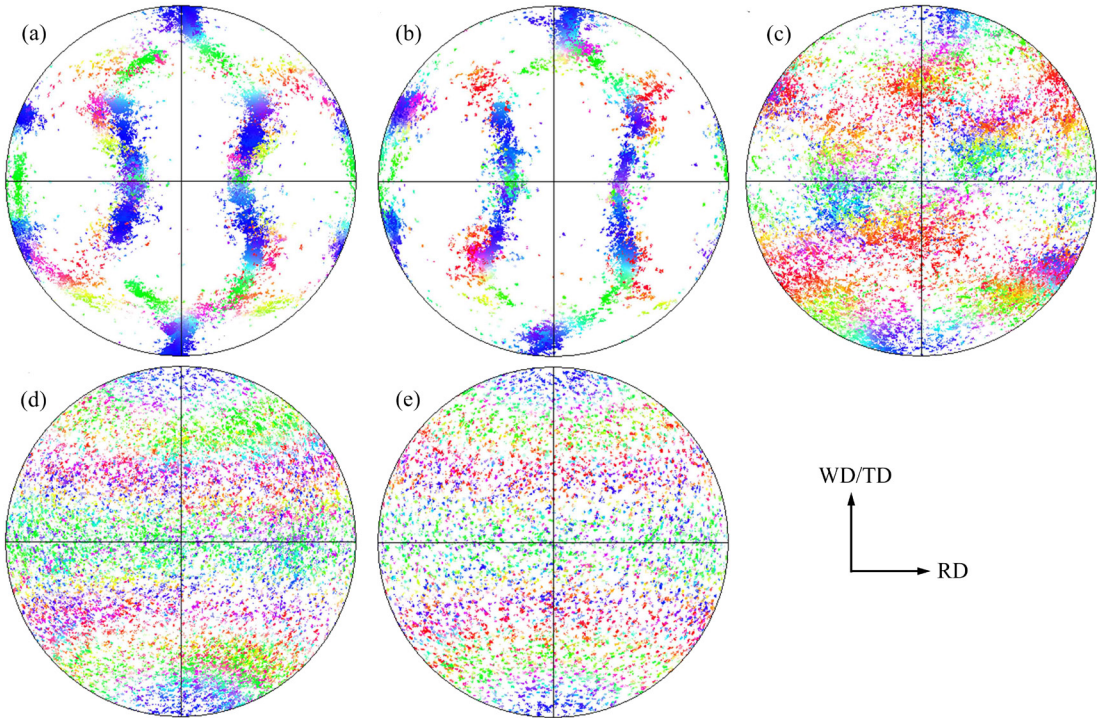

Fig. 6 {111} pole figures of five EBSD results: (a) Area *A*; (b) Area *B*; (c) Area *C*; (d) Area *D*; (e) Area *E*

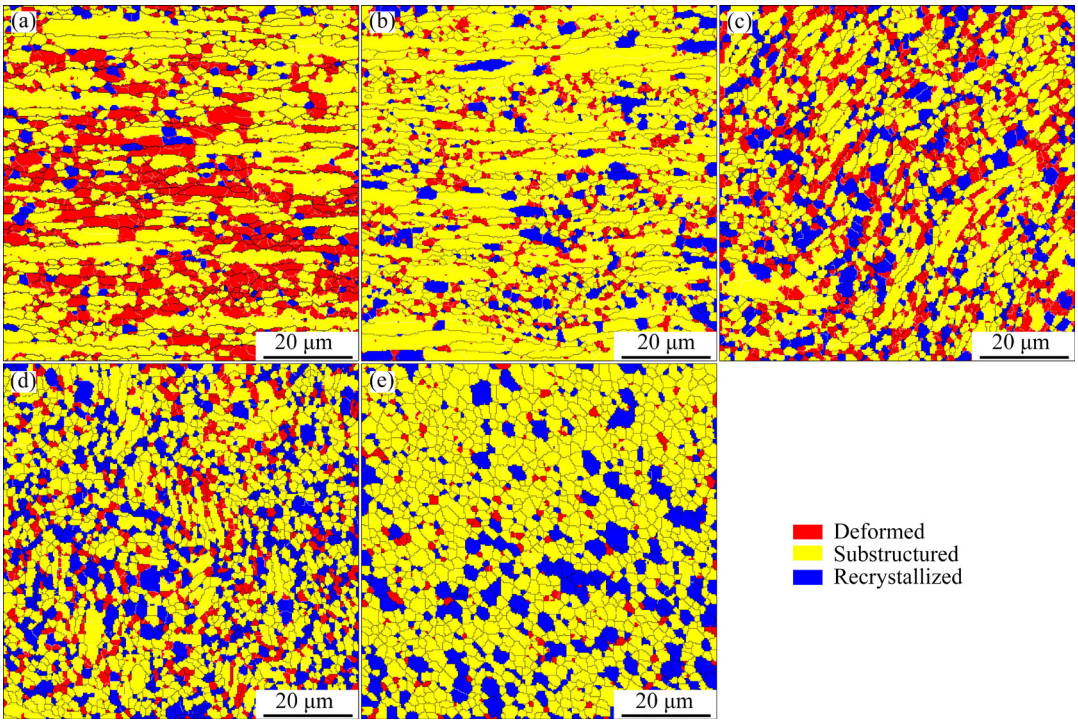

Fig. 7 Recrystallization distribution of different areas in Fig. 2: (a) Area *A*; (b) Area *B*; (c) Area *C*; (d) Area *D*; (e) Area *E*

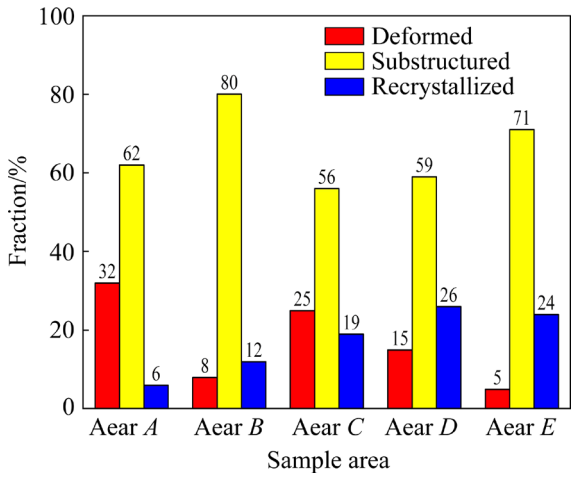

Fig. 8 Recrystallization fraction of different areas in Fig. 2

accounts for the largest part, about 62%, and the deformed structure accounts for 32%. Only 6% of the structure is recrystallized. In the HAZ (Fig. 7(b)), many deformed structures become substructures. The fraction of deformed area is 8% and that of the substructure is 80%. The recrystallization fraction increases to 12%. However, in the TMAZ, the situation has changed. As shown in Fig. 7(c), the deformed proportion increases to 25%, which is more than that in Fig. 7(b). Meanwhile, the recrystallization proportion is also raised to 19%, but the substructure proportion decreases to 56%. In the location closer to the NZ, the Area *D* (Fig. 7(d)), the amount of deformed structure is reduced again (15%), and the proportion of recrystallized structure increased to 26%. The amount of substructures does not change much (59%). Finally, in the NZ (Fig. 7(e)), only 5% of the structure is in deformed condition. The proportion of the substructure increases to 71%, and the proportion of recrystallized grain is 24%. Obviously, as the position gets closer to the welding center, the proportion of deformed structures first decreases, then increases, and finally decreases again. The trend of substructure is just opposite from that of the deformed structure. The recrystallization fraction is low at first, then it gradually rises and maintains at around 25% in the end.

3.3 TEM result

Figure 9 shows the TEM images of different areas. Figure 9(a) shows the BM area. Clearly, this is a typical TEM image of a rolled sheet. Grains are bamboo-liked structures and dislocations are distributed in the grains. Figure 9(b) shows the TEM image of the HAZ. In this image, the overall dislocation density is lower than that in the BM.

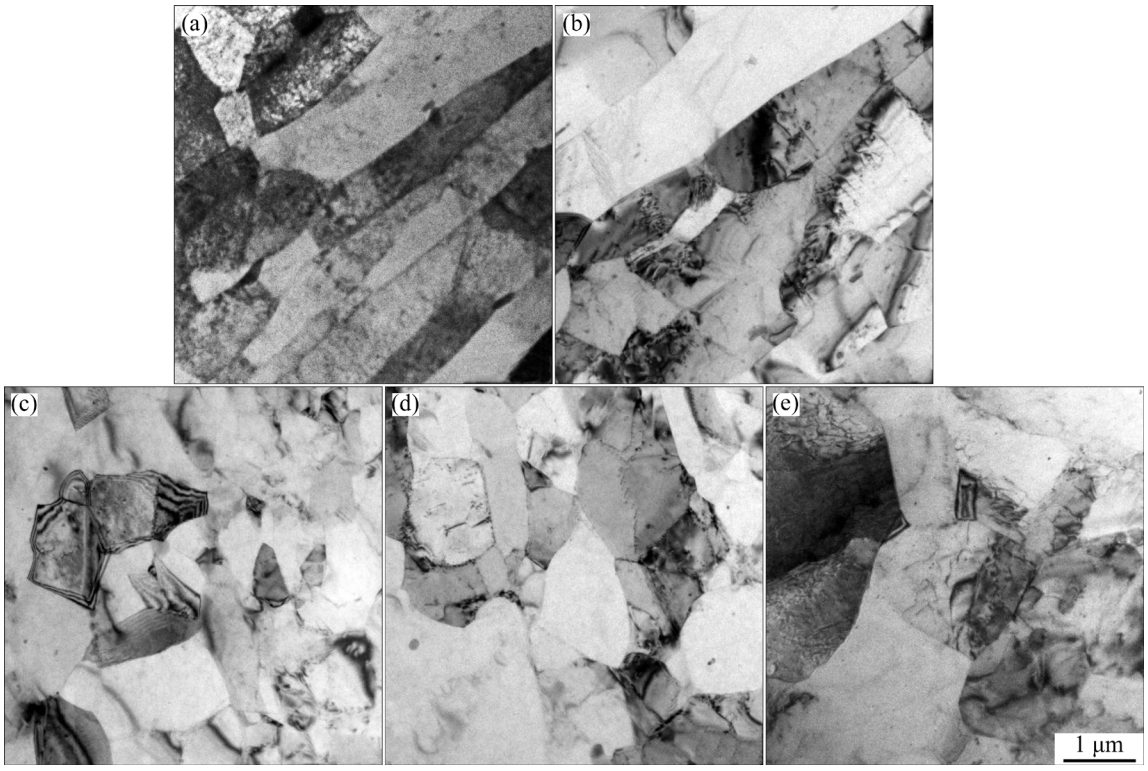

Fig. 9 TEM images of different areas: (a) BM; (b) HAZ; (c) TMAZ far from center; (d) TMAZ close to center; (e) NZ

Recrystallization nucleation appears near the GB of the fiber structure, but the grains have not grown up yet. In the TMAZ near the HAZ (Fig. 9(c)), the recrystallized grains have grown to about 1 μm. The continuous fiber structure begins to be affected by thermoplasticity, becoming discrete. As the location gets closer to the NZ, the recrystallized grains continue to grow, and the size exceeds 1 μm (Fig. 9(d)). Finally, in the NZ (Fig. 9(e)), the fiber structure no longer exists, replaced by equiaxed grains due to dynamic recrystallization. However, there are still many dislocations in the grains in the upper left corner of the figure, and the overall recrystallization fraction is higher.

Figure 10 shows the TEM images of $Al_3(Sc,Zr)$ particles in different area. Figure 10(a) shows the particle in the HAZ. In this area, the particles are uniformly distributed in the grain and the average diameter of the particles is about 10 nm. No dislocation is found inside the grain or around the particles. In the TMAZ far from the NZ (Area *C* in Fig. 2), as shown in Fig. 10(b), several dislocations appear inside the grain and some are pinned by the $Al_3(Sc,Zr)$ particles. The average size of the particles remains around 10 nm and only a few particles grow up. Some particles aggregate together, forming a particle cluster (shown by green arrows). However, things change a lot in the TMAZ close to the NZ (Area *D* in Fig. 2). In Fig. 10(c), the number of dislocations is more than that in the previous samples, and some dislocation walls appear (yellow lines). In addition, many particles are surrounded by dislocations (red dot circles). Except for the dislocations, the situation with particles has also changed. The particle aggregation phenomenon is more common (pointed out by green arrows). The average size of the $Al_3(Sc,Zr)$ particles rises to 10−15 nm. Finally, in the NZ (Area *E* in Fig. 2), the number of dislocations is higher than that in all previous samples. Most particles are surrounded by dislocations (red dot circles). Some dislocations have passed through the particles, leaving Orowan circles around the particles (green arrows). The particle aggregation phenomenon is still very common.

As a comparison, particles in the base material (BM) before FSW are demonstrated in Fig. 11(a). Apparently, the diameter of the particles is 10−15 nm, and the shape of the particles is mainly spherical. For the NZ, the particles grow up a little

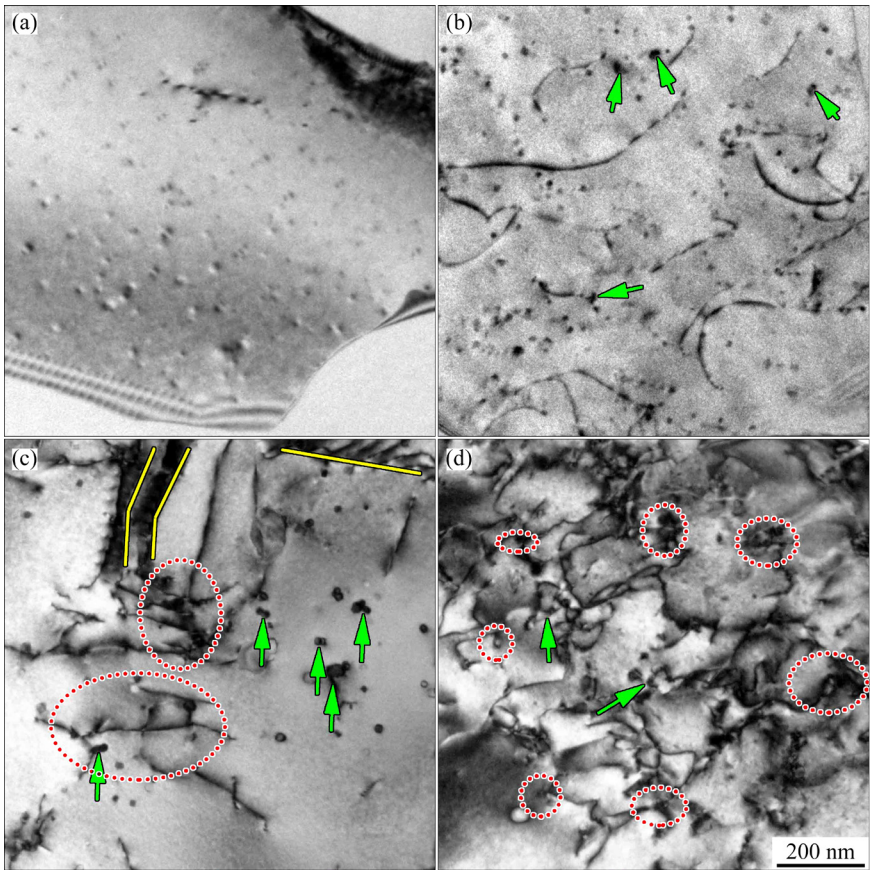

Fig. 10 TEM images of $Al_3(Sc,Zr)$ particles: (a) HAZ; (b) TMAZ far from center; (c) TMAZ close to center; (d) NZ

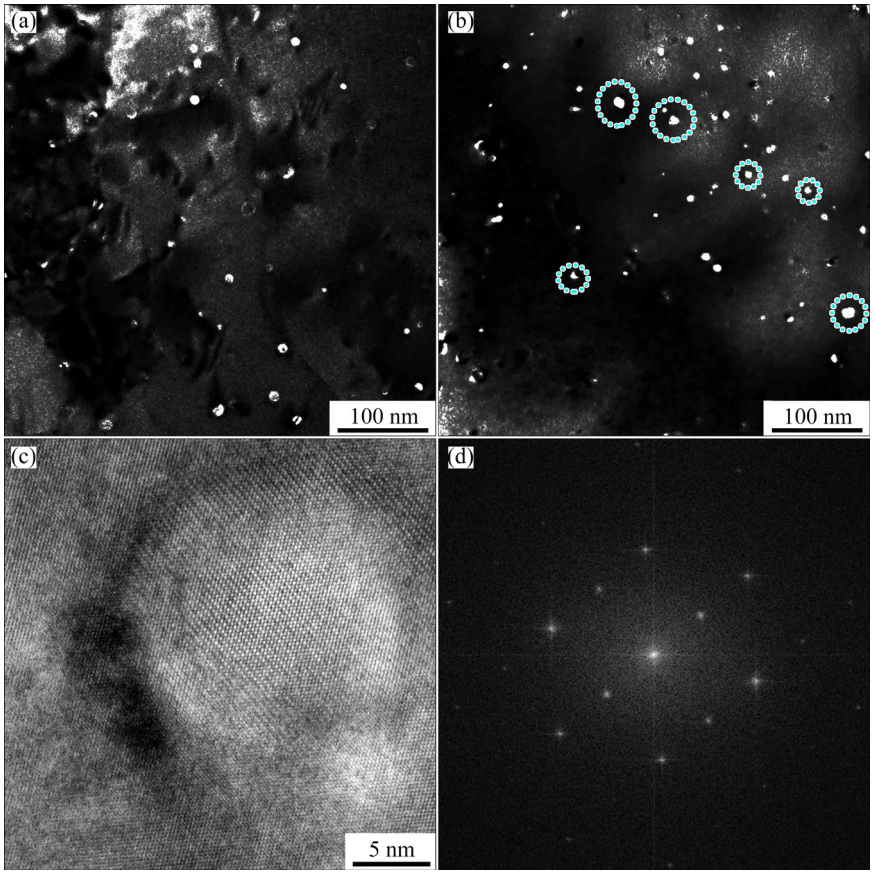

Fig. 11 TEM images of $Al_3(Sc,Zr)$ particles: (a) BM; (b) NZ; (c) HRTEM of particle in BM; (d) FFT

(about 15 nm), but the shape has been changed (Fig. 11(b)). Some polygonal particles appear (blue circles). Figure 11(c) shows the HRTEM of a typical $Al_3(Sc,Zr)$ particle in the BM. The edge of the particle is smooth without strain, indicating that the particle is coherent of the matrix. Typical spots of $L1_2$ structure appear in the Fast Fourier Transformation (FFT).

After the FSW, the change of particles is huge. Most $Al_3(Sc,Zr)$ particles become incoherent with the matrix, and the morphology has changed tremendously. Figure 12 demonstrates three kinds of typical incoherent $Al_3(Sc,Zr)$ particles. Figures 12(a, b, c) are the first one. The particle shape is hexagonal with a length of 20 nm on the diagonal and a distance between parallel sides of 15 nm. Parallel moiré fringes appear inside the particle. It is obvious that the edge of the particle is smooth and no dislocation is found on the edge. Inside the particle, the moiré fringes are due to periodic misalignments of the atomic planes, like screw dislocations (yellow arrows). After FFT, it is found that there are several sets of parallel spots in the ⟨200⟩ direction (Fig. 12(c)). This phenomenon proves that there exist strains inside the particle and the misalignments make the particle lose its coherency with the matrix. Different from the first one, the particle morphology in Fig. 12(d) is more complex. The particle shape is an octagon consisting of four long sides and four short sides, with a diameter of about 20 nm. In addition, there are two sets of staggered moiré patterns in the particle. It can be seen from Fig. 12(e) that the edge is also smooth without any strain. But inside the particle, two sets of screw dislocations intersect in it (yellow lines). Two sets of parallel spots around the main spot can also be seen in the FFT image (Fig. 12(f)), indicating the cross misalignment. Apparently, the internal strain of the particle is stronger than that of the previous one. The third kind of incoherent particle is much different from the former two kinds, as shown in Figs. 12(g, h, i). The shape of the particle is also an octagon composed of four long sides and four short sides. This particle not only has strains inside it but also has a different orientation with the matrix. It can be seen from Fig. 12(h) that the edge of the particle is wide and rough. The rough edge area can be regard

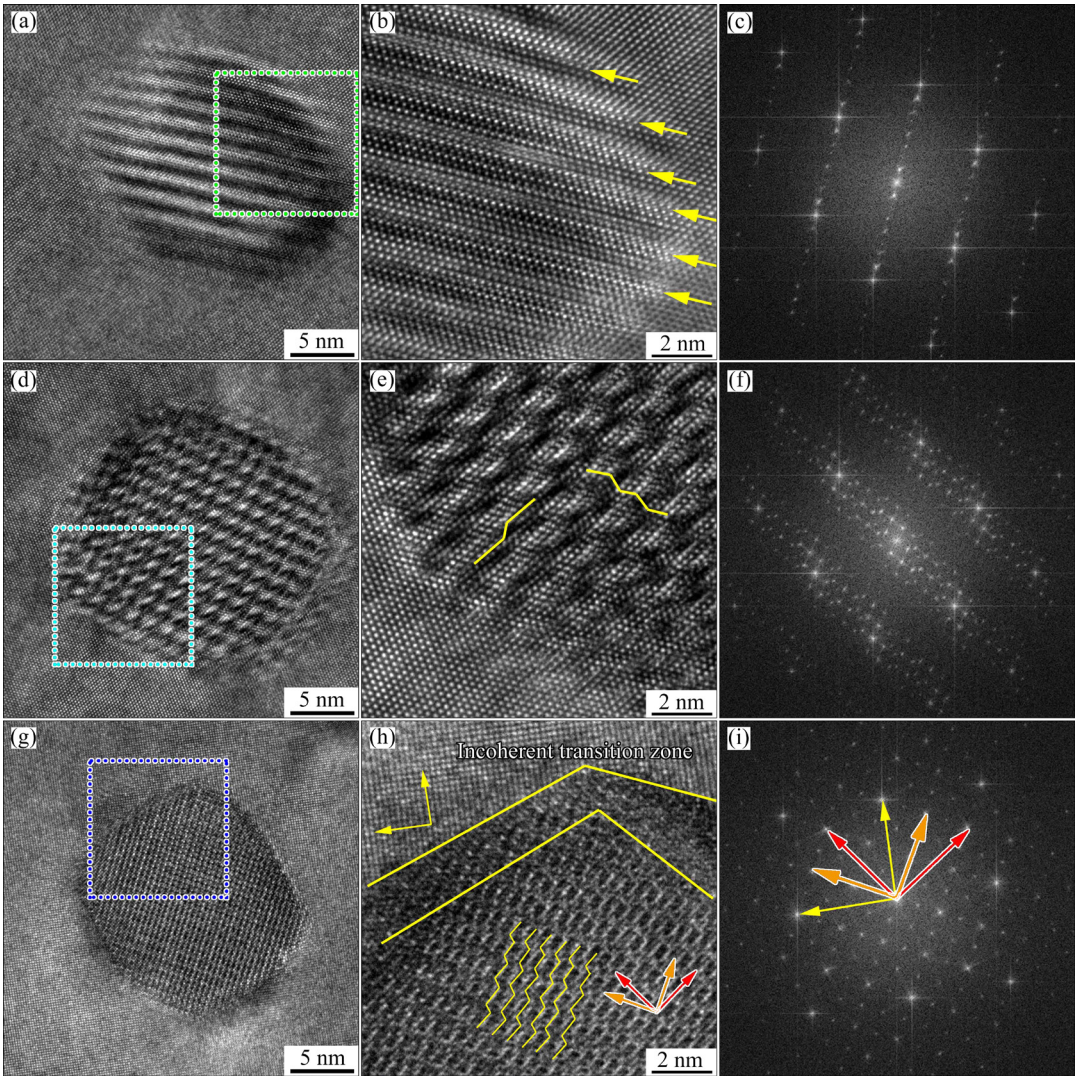

Fig. 12 HRTEM images of typical incoherent $Al_3(Sc,Zr)$ particles: (a, d, g) HRTEM; (b, e, h) HRTEM with higher magnification; (c, f, i) FFT

as an incoherent transition zone for the different orientations. Dense lattice misalignments can be observed and many screw dislocations are made up by these different lattices, indicating the strong internal strain. Also, the FFT image shows that the spot orientation of the particle is different from that of the matrix (Fig. 12(i)), which can also be found in the HRTEM image.

3.4 Mechanical properties

Figure 13 shows the hardness distribution. The hardness of the base metal is about HV 122. Near the center of the weld, the hardness gradually decreases. In the HAZ, the hardness gradually drops to HV 116. In the TMAZ, the hardness of the part far away from the NZ decreases slowly, while in the part close to the NZ, the hardness decreases rapidly. In the NZ, the hardness remains low and stable, fluctuating between HV 102 and HV 106. Figure 14 shows the tensile properties of the samples. The tensile strength (TS) of the base material without FSW is 414 MPa, the yield strength (YS) is 311 MPa, and the elongation is 14.7%. The TS of the FSW sample is 367 MPa, the YS is 263 MPa, and the overall elongation is 10.5%. However, it is worth noting that the fracture occurs in the weld zone. Considering the situation that the BM has higher strength, it can be speculated that the elongation of BM section is much less than that of weld zone, leading to the phenomenon that the overall elongation of FSW sample is less than that of the original sheet. If only the weld area is measured, the actual elongation is about 25%.

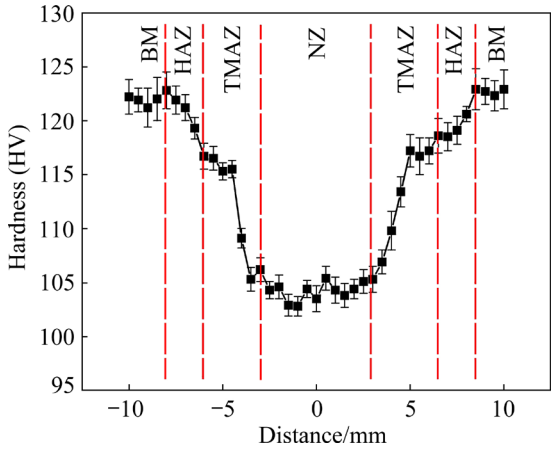

Fig. 13 Microhardness distribution of FSW sheet

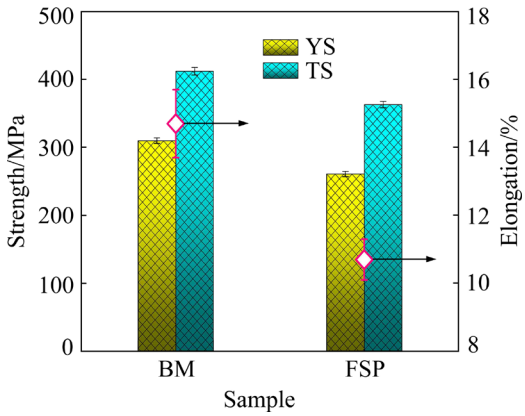

Fig. 14 Tensile properties of samples

4 Discussion

4.1 Grain morphology and recrystallization

From the metallograph and EBSD (Figs. 2−4), it can be clearly seen that as the distance gets closer to NZ, there are more and more recrystallized grains in the fiber structure, and the degree of distortion of the fiber structure also increases. This is because that the influence of heat and plastic deformation will be greater when the location becomes closer to the NZ. Because the nugget area is directly passed through by the probe, the grains are stretched and crushed, and the structure is all fine equiaxed grains. As shown in Fig. 15, due to the rotation of the threads on the probe, material from the front is continuously fed to the back. In the normal direction of the sheet, the thread will rise with rotation, and the fiber particles in the TMAZ will follow the trajectory of the thread, thus bending upwards and outwards. The closer the probe, the greater the impact force, and the greater the bend. The TMAZ is simultaneously subjected to high temperature and plastic deformation, so strong dynamic recrystallization occurs in the structure. The HAZ is far away from the probe, and is less affected by the rotating process. It does not bend significantly and is only affected by the heat transfer. Therefore, only static recrystallization occurs and some little grains are formed in this region.

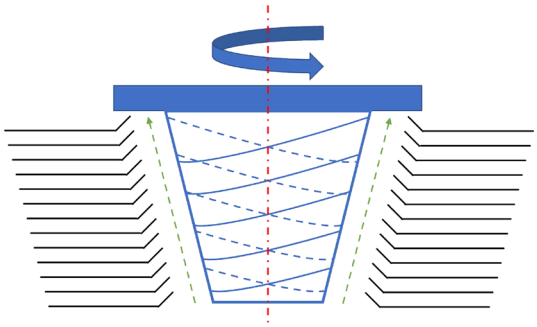

Fig. 15 Schematic diagram of impact of FSW on microstructure

Additionally, the change of recrystallization fraction is also related with the friction stir deformation. As shown in Fig. 6, the proportion of deformed structure, substructure and recrystallized structure does not change regularly with the position. For the deformed structure and the substructure, there is no doubt that the amount of deformed structure in the original sheet is the largest. In the HAZ, affected by the high temperature of FSW, many dislocations have recovered, so the deformed proportion decreases. However, the welding heat is not enough for complete recrystallization. Therefore, many substructures are formed. In the TMAZ adjacent to the HAZ, new deformations are introduced to the sheet but the short-term heat cannot annihilate the newly-introduced deformation. As a result, the deformation fraction increases and the substructure fraction decreases. In the position closer to the NZ, the temperature is higher and the deformation becomes severer. Thus, the driving force for the recrystallization is larger. Consequently, the preserved deformation is less and more structures turn to substructures. Finally, in the NZ, the deformation-driven metallurgy with high plastic strain and frictional/deformation heat contributes to dynamic recovery and dynamic recrystallization [27]. Hence, the deformed structure continues to decrease and the substructures continues to increase. During the FSW, rapid dynamic recovery occurs

readily, which generally prevents the accumulation of sufficient dislocations to sustain dynamic recrystallization. Therefore, in the NZ, many substructures are formed rather than a fully recrystallized structure, explaining the phenomenon that the recrystallization fraction is not always elevated with the change of position.

4.2 Al_3(Sc,Zr) particles

Apparently, the size and coherency of Al_3(Sc,Zr) particles change. After the FSW, the Al_3(Sc,Zr) particles in the NZ have grown up and most particles have lost the coherency with the Al matrix. For the coarsening of the particle, this is because that a lot of heat is generated during welding. High temperature would accelerate the diffusion rate of solute atoms, making the second phase particles grow up [28]. At the same time, FSW generates a large number of lattice defects such as dislocations, and many dislocations are pinned by particles, and these defects can become diffusion channels of solute elements. As a result, under the coupling effects of high temperature and large number of defects, the Al_3(Sc,Zr) particles would grow up.

However, the particles not only grow, but also lose coherency. The incoherent particles have different morphologies too. According to the previous research [29], there exist three types of coherency loss by severe plastic deformation and heat. In this work, the coherency loss can be summarized as two types. The first type of the coherency loss is shown in Figs. 12(a) and (d). This coherency loss is due to the particles being passed through dislocations or grain boundaries. There are obvious moiré patterns in these particles, which means that the strain of the particles causes lattice misalignment. The morphology of the pattern appearing inside the particle is similar to screw dislocation. Other researchers have also found the similar phenomenon [30]. After being passed through a large number of dislocations or grain boundaries, moiré patterns and lattice misalignments are introduced into the particles. Strong recovery and recrystallization by SPD greatly raise the probability of dislocations or grain boundaries passing through Al_3(Sc,Zr) particles. Therefore, after the FSW, lattice misalignments would appear and many Al_3(Sc,Zr) particles would lose coherency with the Al matrix. Furthermore, the particles shown in Fig. 12(g) demonstrate a different kind of incoherency, the interface-bypass incoherency. This is because that the particles are bypassed by the grain boundary. During the strong dynamic recrystallization, the motion of grain boundaries is very intensive. Under this condition, there would be several particles bypassed by grain boundaries instead of cut through it. After being bypassed by the grain boundaries, the particles come into a new grain which has a different orientation compared with the original grain. However, the particles maintain their original orientation. So, there is an orientation difference between the particles and the grain, leading to the loss of coherency.

4.3 Mechanical properties of FSW sheet

Hardness decreases with distance from NZ. Partial recrystallization of HAZ occurs. As the position gets closer and closer to the center, The temperature would become higher and higher, so is the recrystallization fraction. In TMAZ, the hardness decreases slowly in the part far from the NZ, while the hardness decreases more rapidly in the part close to the NZ. In the part far away from the NZ, the integrity of the fiber structure is not destroyed. The main change of the microstrucure is bending and partial recrystallization, so its hardness is slowly reduced. In the part close to the NZ, the fibrous structure is destroyed, mixed with some equiaxed grains, and the degree of recrystallization increases rapidly due to stronger mechanical impact and higher temperature, so the hardness drops rapidly. The more the equiaxed grain, the lower the hardness. In the NZ, the microstructure is dominated by small equiaxed grains due to strong recovery and recrystallization. In the NZ, the dislocation density is low, and the work hardening effect has been eliminated compared to the BM and the TMAZ. Thus, NZ has the lowest hardness.

For tensile properties, the factors that may give rise to the difference in the strength between the BM and the FSW sheet are GB and Al_3(Sc,Zr) particles. It is clear that the recrystallized structure and the size of the Al_3(Sc,Zr) particles are different in the samples. In addition, it is necessary to consider the contribution of the HAGB and the LAGB. The contribution of the HAGB and the LAGB to the strength is different. The YS that introduced by GB can be described as [31,32].

$$\sigma_{GB}=\sigma_{HAGB}+\sigma_{LAGB}=k_y d_{HAGB}^{-1/2}+M\alpha_1 G(1.5bS_v\theta_{av}^{LAGB}f_{LAGB})^{1/2} \quad (1)$$

where k_y is the Hall−Petch constant, about 100 MPa·μm$^{0.5}$ [33]; d_{HAGB} is the size of grains with HAGB; M is the Taylor factor equaling to 3; α_1 is a constant, which is 0.3 in this equation [32]; G is the shear modulus of Al alloy (26 GPa); b is the magnitude of the Burger vector of the matrix, 0.286 nm in Al alloy; S_v represents the total area of grain boundaries per unit volume; θ_{av}^{LAGB} is the average misorientation angle of the LAGB; f_{LAGB} is the proportion of the LAGBs. Considering situation that the fracture of FSW sheet happens in the NZ, the data of NZ can represent the actual result of FSW sheet. In the same way, the data of BM can represent the result of original sheet. The GB data of BM and NZ obtained from the EBSD results and the calculated strengths are listed in Table 1.

Table 1 EBSD results and calculated strength

Sample	d_{HAGB}/μm	S_v/μm^{-1}	θ_{av}^{LAGB}/(°)	f_{LAGB}/%	σ_{HAGB}/MPa	σ_{LAGB}/MPa	σ_{GB}/MPa
BM	4.29	0.77	4.34	41.78	48	81	129
NZ	2.55	0.51	8.66	6.69	63	37	100

Obviously, according to the calculated result, the small grain size of grains with HAGB of the FSW sheet contributes more strength compared with that of BM. However, less LAGB fraction and few GB amount make the FSW sheet at a disadvantage in comparison with the strength of the BM.

Furthermore, the YS is not only affected by GBs, but also the effect of $Al_3(Sc,Zr)$ particle should be discussed. Generally, the strength by the $Al_3(Sc,Zr)$ particles is divided into two types. One is coherency strengthening and modulus hardening, and the other is Orowan mechanism. These strengths are based on coherent $Al_3(Sc,Zr)$ particles. According to HUANG et al [34], when the diameter of the $Al_3(Sc,Zr)$ particles is less than 10 nm, the strengthening mechanism is mainly the first type. If the diameter of the $Al_3(Sc,Zr)$ particles is over 10 nm, the second type will account for the strengthening. In this work, the size of most $Al_3(Sc,Zr)$ particles is over 10 nm. The strengthening equation from the particle is as follows [35−37]:

$$\sigma_{or}=kM\frac{Gb}{(1-\nu)^{1/2}}\frac{\ln(D_s/b)}{\lambda} \quad (2)$$

where k≈0.127 in mono-dispersed particle; ν is Poisson ratio of the matrix (0.34 in Al−Mg matrix); D_s is the mean diameter of a circular cross-section in a random plane for a spherical precipitate (D_s=πD_{av}/4), where D_{av} is the average diameter the particles; λ is the effective inter-particle distance ($\lambda=D_s(1/2\sqrt{2\pi/(3f_v)}-1)$) [37], where f_v is the volume fraction of the particles. The data obtained from the TEM images and the calculated strength are demonstrated in Table 2.

Table 2 TEM results and calculated strength

Sample	D_{av}/nm	f_v/%	D_s/nm	λ/nm	σ_{or}/MPa
BM	11.9	0.22	9.3	134.9	91
NZ	13.2	0.22	10.4	149.7	84

In Table 2, the calculated strength is given. The contribution of $Al_3(Sc,Zr)$ particles to the YS is similar in the two samples. Clearly, the change of $Al_3(Sc,Zr)$ particles in the NZ has a little influence on the mechanical property and the main difference is from the GB strengthening. In addition, the strength of the alloy should also consider the threshold stress in pure Al (σ_0) and the effect of solid solution of Mg atoms (σ_{SS}). These two factors are same as the BM and the NZ. The threshold stress in pure Al is about 10 MPa and the solution strengthening efficiency of Mg solutes is taken to be 13.8 MPa/% Mg [25]. The strength comparison is listed in Table 3. Obviously, the calculated results are basically consistent with the actual results.

Table 3 Comparison of calculated data and actual result

Sample	σ_0/MPa	σ_{SS}/MPa	σ_{GB}/MPa	σ_{or}/MPa	Actual/MPa	Measured/MPa
BM	10	83	129	91	313	311
NZ	10	83	100	84	277	263

5 Conclusions

(1) As the position gets closer and closer to the center, the fibers are bent more and more severely, and the average grain misorientation becomes larger and larger. The newly evolved grains have nearly random crystallographic orientations, making the texture gradually disappear. The grain size in the

NZ of the FSW sheet is 2.31 μm.

(2) Most $Al_3(Sc,Zr)$ particles in the NZ of the FSW sheet lose coherency with the matrix due to the strong dynamic recovery and recrystallization. The shape of incoherent particles changes from spherical to polyhedron. There exist inner strains inside the incoherent particles and some particles even have different orientations with the matrix.

(3) The tensile strength of the base material without FSW is 414 MPa, and the yield strength is 311 MPa. The tensile strength of the FSW sheet is 367 MPa, and the yield strength is 263 MPa.

References

[1] JIANG Jing-yu, JIANG Feng, ZHANG Meng-han, XU Pian, TANG Zhong-qin, TONG Meng-meng. Effects of annealing under fixed temperature and cyclic temperature on strength and microstructure of Al–Mg–Mn−Sc−Zr alloy [J]. Materials Science and Engineering: A, 2019, 764: 138275.

[2] SUKIMAN N L, GUPTA R K, ZHANG R, BUCHHEIT R G, BIRBILIS N. Influence of microalloying additions on Al−Mg alloy. Part 2: Phase analysis and sensitisation behavior [J]. Corrosion Engineering Science and Technology, 2014, 49: 263−268.

[3] POLMEAR I J. Light alloys: Metallurgy of the light metals [M]. New York: Wiley & Sons, 1995.

[4] XIAO Quan-feng, HUANG Ji-wu, JIANG Ying-ge, JIANG Fu-qin, WU Yun-feng, XU Guo-fu. Effects of minor Sc and Zr additions on mechanical properties and microstructure evolution of Al−Zn−Mg−Cu alloys [J]. Transactions of Nonferrous Metals Society of China, 2020, 30(6): 1429−1438.

[5] ZHEMCHUZHNIKOVA D, KAIBYSHEV R. Mechanical behavior of an Al−Mg−Mn−Sc alloy with an ultrafine grain structure at cryogenic temperatures [J]. Advanced Engineering Materials, 12015, 17: 1804−1811.

[6] CHUVIL'DEEV V N, GRYAZNOV M Y, SHOTIN S V, KOPYLOV V I, NOKHRIN A V, LIKHNITSKII C V, MURASHOV A A, BOBROV A A, TABACHKOVA N Y, PIROZHNIKOVA O E. Investigation of superplasticity and dynamic grain growth in ultrafine-grained Al−0.5%Mg−Sc alloys [J]. Journal of Alloys and Compounds, 2021, 877: 160099.

[7] JIANG Feng, ZHOU Jiang, HUANG Hong-feng, QU Ji-ping. Characterization of microstructure and mechanical properties in Al−Mg alloy with addition of Sc and Zr [J]. Materials Research Innovations, 2015, 18: 228−234.

[8] XU Pian, JIANG Feng, MENG Song, YI Ke-ke, JIANG Jing-yu, CAO Qin-xuan, PENG Yong-yi. Microstructure and mechanical properties of Al−Mg−Sc−Zr alloy variable polarity plasma arc welding joint [J]. Journal of Materials Engineering and Performance, 2018, 27: 4783−4790.

[9] GAO Qing-wei, SHU Feng-yuan, HE Peng, DU Wen-bo. Microstructure and impact mechanical properties of multi-layer and multi-pass TIG welded joints of Al−Zn−Mg alloy plates [J]. Transactions of Nonferrous Metals Society of China, 2019, 29(12): 2496−2505.

[10] HAN Yi-long, XUE Song-bai, FU Ren-li, ZHANG Peng. Effect of hydrogen content in ER5183 welding wire on the tensile strength and fracture morphology of Al−Mg MIG weld [J]. Vacuum, 2019, 166: 218−225.

[11] XU R Z, LI H, HOU Y X, WEI Z C, LI F S, CUI S L, LIU X H. Influencing mechanism of Al−Zn coating addition on interfacial microstructure and mechanical property of vacuum electron beam welded Mg/steel joint [J]. Vacuum, 2018, 158: 31−38.

[12] HE Zhen-bo, PENG Yong-yi, YIN Zhi-min, LEI Xue-feng. Comparison of FSW and TIG welded joints in Al−Mg−Mn−Sc−Zr alloy plates [J]. Transactions of Nonferrous Metals Society of China, 2011, 21(8): 1685−1691.

[13] MISHRA R S, MA Z Y. Friction stir welding and processing [J]. Materials Science and Engineering R, 2005, 50: 1−78.

[14] MENG Xiang-chen, HUANG Yong-xian, CAO Jian, SHEN Jun-jun, DOS SANTOS J F. Recent progress on control strategies for inherent issues in friction stir welding [J]. Progress in Materials Science, 2021, 115: 100706.

[15] MIRZADEH H. High strain rate superplasticity via friction stir processing (FSP): A review [J]. Materials Science and Engineering A, 2021, 819: 141499.

[16] KALINENKO A, VYSOTSKIY I, MALOPHEYEV S, MIRONOV S, KAIBYSHEV R. New insight into the phenomenon of the abnormal grain growth in friction-stir welded aluminum [J]. Materials Letters, 2021, 302: 130407.

[17] TOURSANGSARAKI M, LI Q, HU Y X, WANG H M, ZHAO D, ZHAO Y B. Crystal plasticity modeling for mechanical property prediction of AA2195-T6 friction stir welded joints [J]. Materials Science and Engineering A, 2021, 823: 141677.

[18] ZHEMCHUZHNIKOVA D, MALOPHEYEV S, MIRONOV S, KAIBYSHEV R. Cryogenic properties of Al−Mg−Sc−Zr friction-stir welds [J]. Materials Science and Engineering A, 2014, 598: 387−395.

[19] KULITSKIY V, MALOPHEYEV S, MIRONOV S, KAIBYSHEV R. Grain refinement in an Al−Mg−Sc alloy: Equal channel angular pressing versus friction-stir processing [J]. Materials Science and Engineering A, 2016, 674: 480−490.

[20] BESEL Y, BESEL M, ALFARO MERCADO U, KAKIUCHI T, HIRATA T, UEMATSU Y. Influence of local fatigue damage evolution on crack initiation behavior in a friction stir welded Al−Mg−Sc alloy [J]. International Journal of Fatigue, 2017, 99: 151−162.

[21] CHHANGANI S, MASA S K, MATHEW R T, PRASAD M J N V, SUJATA M. Microstructural evolution in Al−Mg−Sc alloy (AA5024): Effect of thermal treatment, compression deformation and friction stir welding [J]. Materials Science and Engineering A, 2020, 772: 138790.

[22] LIU Xiao-chao, ZHEN Yun-qian, SUN Yu-feng, SHEN Zhi-kang, CHEN Hai-yan, GUO Wei, LI Wen-ya. Local inhomogeneity of mechanical properties in stir zone of friction stir welded AA1050 aluminum alloy [J]. Transactions of Nonferrous Metals Society of China, 2020, 30(9): 2369−2380.

[23] TAO Y, ZHANG Z, NI D R, WANG D, XIAO B L, MA Z Y. Influence of welding parameter on mechanical properties and fracture behavior of friction stir welded Al−Mg−Sc joints [J]. Materials Science and Engineering A, 2014, 612: 236−245.

[24] MALOPHEYEV S, KULITSKIY V, MIRONOV S, ZHEMCHUZHNIKOVA D, KAIBYSHEV R. Friction-stir welding of an Al−Mg−Sc−Zr alloy in as-fabricated and

work-hardened conditions [J]. Materials Science and Engineering A, 2014, 600: 159−170.
[25] VYSOTSKIY I, ZHEMCHUZHNIKOVA D, MALOPHEYEV S, MIRONOV S, KAIBYSHEV R. Microstructure evolution and strengthening mechanisms in friction-stir welded Al−Mg−Sc alloy [J]. Materials Science and Engineering A, 2020, 770: 138540.
[26] KALASHNIKOVA T, CHUMAEVSKII A, KALASHNIKOV K, FORTUNA S, KOLUBAEV E, TARASOV S. Microstructural analysis of friction stir butt welded Al−Mg−Sc−Zr alloy heavy gauge sheets [J]. Metals, 2020, 10: 806.
[27] XIE Yu-ming, MENG Xiang-chen, CHANG Yue-xin, MAO Dong-xin, YANG Yu-chen, XU Yan-li, WAN Long, HUANG Yong-xian. Ameliorating strength−ductility efficiency of graphene nanoplatelet-reinforced aluminum composites via deformation-driven metallurgy [J]. Composites Science and Technology, 2022, 219: 109225.
[28] XU Pian, JIANG Feng, TANG Zhong-qin, YAN Ning, JIANG Jing-yu, XU Xu-da, PENG Yong-yi. Coarsening of Al_3Sc precipitates in Al−Mg−Sc alloys [J]. Journal of Alloys and Compounds, 2019, 781: 209−215.
[29] JIANG Jing-yu, JIANG Feng, ZHANG Meng-han, TANG Zhong-qin, TONG Meng-meng. Al_3(Sc,Zr) precipitation in deformed Al−Mg−Mn−Sc−Zr alloy: Effect of annealing temperature and dislocation density [J]. Journal of Alloys and Compounds, 2020, 831: 154856.
[30] BURANOVA Y, KULITSKIY V, PETERLECHNER M, MOGUCHEVA A, KAIBYSHEV R, DIVINSKI S V, WILDE G. Al_3(Sc,Zr)-based precipitates in Al−Mg alloy: Effect of severe deformation [J]. Acta Materialia, 2017, 124: 210−224.
[31] ZHANG Xiao-dan, HANSEN N, GAO Yu-kui, HUANG Xiao-xu. Hall−Petch and dislocation strengthening in graded nanostructured steel [J]. Acta Materialia, 2012, 60(16): 5933−5943.
[32] TANG Lei, PENG Xiao-yan, HUANG Ji-wu, MA Ai-bin, DENG Ying, XU Guo-fu. Microstructure and mechanical properties of severely deformed Al−Mg−Sc−Zr alloy and their evolution during annealing [J]. Materials Science and Engineering A, 2019, 754: 295−308.
[33] FURUKAWA M, HORITA Z, NEMOTO M, VALIEV R Z, LANGDON T G. Microhardness measurements and the Hall−Petch relationship in an Al−Mg alloy with submicrometer grain size [J]. Acta Materialia, 1996, 44(11): 4619−4629.
[34] HUANG Hong-feng, JIANG Feng, ZHOU Jiang, WEI Li-li, QU Ji-ping, LIU Le-le. Effects of Al_3(Sc,Zr) and shear band formation on the tensile properties and fracture behavior of Al−Mg−Sc−Zr alloy [J]. Journal of Materials Engineering and Performance, 2015, 24: 4244−4252.
[35] FULLER C B, SEIDMAN D N, DUNAND D C. Mechanical properties of Al(Sc,Zr) alloys at ambient and elevated temperatures [J]. Acta Materialia, 2003, 51(16): 4803−4814.
[36] KENDIG K L, MIRACLE D B. Strengthening mechanisms of an Al−Mg−Sc−Zr alloy [J]. Acta Materialia, 2002, 50(16): 4165−4175.
[37] SENKOV O N, SHAGIEV M R, SENKOVA S V, MIRACLE D B. Precipitation of Al_3(Sc,Zr) particles in an Al−Zn−Mg−Cu−Sc−Zr alloy during conventional solution heat treatment and its effect on tensile properties [J]. Acta Materialia, 2008, 56(15): 3723−3738.

Al−Mg−Sc−Zr 合金搅拌摩擦焊板材的显微组织演变及力学性能

蒋靖宇[1]，姜 锋[2,3,4]，张梦晗[2]

1. 中南大学 冶金与环境学院，长沙 410083；
2. 中南大学 材料科学与工程学院，长沙 410083；
3. 中南大学 轻合金研究院，长沙 410083；
4. 中南大学 轻质高强结构材料国防科技重点实验室，长沙 410083

摘 要：对 Al−Mg−Sc−Zr 合金轧制板材进行搅拌摩擦焊，焊针转速为 500 r/min，行进速度为 100 mm/min。采用 OM、EBSD 和 TEM 对搅拌摩擦焊后的合金板材组织进行表征，并测试显微硬度和拉伸强度。结果表明，搅拌摩擦焊后，旋转焊针附近区域的纤维晶粒发生弯曲；轧制板材的织构逐渐减轻。在焊核区，细小的等轴晶尺寸仅为 2.31 μm。Al_3(Sc,Zr)粒子受到 FSW 的影响。搅拌摩擦焊后的粒子分布和粒子大小与原始板材不同。此外，Al_3(Sc,Zr)粒子的形状由球形变为多边形，许多粒子与 Al 基体变得不共格。搅拌摩擦焊板材的抗拉强度为 367 MPa，屈服强度为 263 MPa，原板材的强度分别为 414 MPa 和 311 MPa。

关键词：Al−Mg−Sc−Zr 合金；搅拌摩擦焊；动态再结晶；Al_3(Sc,Zr)粒子；强度

(Edited by Xiang-qun LI)